AIMS Materials Science, 4(6): 1289-1304.
DOI: 10.3934/matersci.2017.6.1289
Received: 02 October 2017
Accepted: 27 November 2017
Published: 05 December 2017

http://www.aimspress.com/journal/Materials

Research article

Helium Ion Microscopy of proton exchange membrane fuel cell electrode structures

Serguei Chiriaev [1], Nis Dam Madsen [1], Horst-Günter Rubahn [1], and Shuang Ma Andersen [2,*]

[1] The Mads Clausen Institute, University of Southern Denmark, Alsion 2, DK-6400 Sønderborg, Denmark
[2] Department of Chemical Engineering, Biotechnology and Environmental Technology, University of Southern Denmark, Campusvej 55, DK-5230 Odense M, Denmark

* **Correspondence:** Email: mashu@kbm.sdu.dk.

Abstract: Characterization of composite materials with microscopy techniques is an essential route to understanding their properties and degradation mechanisms, though the observation with a suitable type of microscopy is not always possible. In this work, we present proton exchange membrane fuel cell electrode interface structure dependence on ionomer content, systematically studied by Helium Ion Microscopy (HIM). A special focus was on acquiring high resolution images of the electrode structure and avoiding interface damage from irradiation and tedious sample preparation. HIM demonstrated its advantages in surface imaging, which is paramount in studies of the interface morphology of ionomer covered or absorbed catalyst structures in a combination with electrochemical characterization and accelerated stress test. The electrode porosity was found to depend on the ionomer content. The stressed electrodes demonstrated higher porosity in comparison to the unstressed ones on the condition of no external mechanical pressure. Moreover, formation of additional small grains was observed for the electrodes with the low ionomer content, indicating Pt redeposition through Ostwald ripening. Polymer nanofiber structures were found in the crack regions of the catalyst layer, which appear due to the internal stress originated from the solvent evaporation. These fibers have fairly uniform diameters of a few tens of nanometers, and their density increases with the increasing ionomer content in the electrodes. In the hot-pressed electrodes, we found more closed contact between the electrode components, reduced particle size, polymer coalescence and formation of nano-sized polymer fiber architecture between the particles.

Keywords: proton exchange membrane fuel cells (PEMFCs); Helium Ion Microscopy (HIM); interfaces; electrode structure; degradation mechanism

1. Introduction

With the ever-increasing demand for next generation sustainable energy conversion technologies, it is undoubted that the substitution of economic and sustainable clean energy for traditional fossil fuels is becoming a necessity [1,2]. Fuel cells are clean, efficient and renewable energy conversion devices that can directly convert the chemical energy of fuels to electricity through electrochemical processes [3,4]. Especially proton exchange membrane fuel cells (PEMFCs) have demonstrated their powerful potential and are believed to be one of the most promising future energy providers for potable as well as stationary applications [5]. In the past three decades, vast research activities were carried out to boost the final steps for fuel cells to enter the daily life with affordable price and stable performance [6].

Though still not well understood, surface chemistry and morphology of the fuel cell electrode, are crucial parameters influencing the cell performance [7,8]. The delicate three-phase boundary (TPB), where proton, electron and gas meet and initiate the electrochemical reactions, has great influence on the catalyst utilization and cell lifetime. Typically, the thickness of the catalyst layer (CL) is only around 20 μm, which is usually less than 5% of the total thickness of a typical membrane electrode assembly (MEA). CL is the heart of PEMFC, and is responsible for hydrogen oxidation reaction and oxygen reduction reaction. State of the art PEMFC catalyst layer consists of platinum supported by high surface area carbon and impregnated with proton conducting ionomer, e.g., Nafion®, by DuPont.

To maximize electrochemical reaction zone, ionomer component is routinely impregnated in the electrode structure. The loading of the ionomer is usually in a range of 30–50% by weight [9,10], or 10–25% by volume. Based on the earlier studies [11,12,13], the Nafion ionomer was found to have strong affinity towards the catalysts. An ionomer layer (Nafion thin film) is readily formed on top of the catalyst surface. This thin layer is largely responsible for the transport of proton, which is essential for the electrochemical reactions. Besides, the polymer phase can directly influence the morphology of the other two phases. Stability of the polymer or the overall interphase structure in the catalyst layer can be a bottle neck of the fuel cell lifetime challenge.

The Nafion thin film in the CL is of thickness less than 10 nm. This thin film is of a significantly different structure and property comparing to the bulk membrane as reported by many groups and it is an active topic in the field [14,15]. Due to its light elements and minute thickness, Nafion ionomer in CLs is rather difficult to be observed with the most common microscopy techniques [16,17], since the ionomer appears transparent or damaged during observation, which is a well-documented challenge [18]. Visualization of the polymer in these cases often requires tedious preparation procedures, such as staining with heavy metal ions [19], by which the true electrode structure can be compromised. Other characterization methods include various spectroscopies (such as Raman [20] and infrared [21]), nuclear magnetic resonance [11,12,13] and X-ray photoelectron spectroscopy. However, all of them lack information regarding the morphology of electrodes in three dimensions.

Nafion is a well-known dielectric with a high electrical resistivity [22]. When a Nafion sample is investigated in a scanning electron microscope (SEM), this usually results into a rapid charge build-up in the sample, which can disturb its imaging. The other negative aspect of the electron probe beams is image artefacts brought by high radiation damage generated in the polymer materials through the ionization losses of the incident electrons. Even though low energy electron beams can

be used to minimize these effects through overall charge balance [23], an electric field can still be present at the specimen's surface and cause image artefacts. Moreover, as the secondary electron emission depends on the electron beam incidence angle, for structures with large topography variations, such as our electrodes, this approach for charging reduction can have only limited success [24].

In general, Helium Ion Microscopy (HIM) is similar to SEM but instead of a focused electron beam a focused beam of positively charged helium ions is used [25,26]. Hence, in contrast to the negative charging specific to SEM, HIM imaging results in only positive charging, that can be compensated with an electron flood gun. Other significant advantages of HIM in imaging of composite structures include its superior spatial resolution (close to 0.3 nm) a depth-of-field that is about five times larger than that of SEM and an enhanced surface sensitivity [26,27]. In this work, we have used HIM for the characterization of uncoated polymer fuel cell electrodes, in a combination with other experimental techniques, such as the electrochemical characterization and accelerated stress test.

2. Materials and Methods

Catalyst powder from Johnson Matthey, Hispec 9100, was used as received. The powder contained 57 wt% of Pt black nano-particles with a diameter around 3–4 nm and supported on high surface area carbon. The catalyst ionomer electrode was a composite of the catalyst powder and Nafion ionomer (from Ion Power, Inc). The catalyst and the ionomer were homogeneously mixed in a water and ethanol mixture (1:3), with an ultrasonic horn for 10–15 min. Then, the ink was spray printed with an air brush (NEO FOR IWATA HP-TRN1 0.35MM) on a gas diffusion layer (SIGRACET® 36 BD) placed on a heating plate at a temperature of 60 °C.

The HIM study was performed with a Zeiss ORION NanoFab Helium Ion Microscope operating at a beam energy of 30 keV. The scanning electron microscopy (SEM) was performed with a Hitachi S-4800 system with a cold field-emission electron source for ultra-high resolution, and at a beam energy of 5 keV. The transmission electron microscopy (TEM) was performed using a double-aberration corrected JEOL 2200FS (JEOL, Japan) microscope equipped with a field emission gun (FEG). Image processing and analysis were assisted by using Scanning Probe Image Processor (SPIP) and Origin Pro 9.1 software.

The electrochemical measurements were carried out in a traditional three-electrode electrochemical cell. The electrochemical accelerated stress test (AST) was performed by potential cycling as a simulated start/stop test [28]. The AST was carried out between 0.4 and 1.6 V with a scan rate of 1 V s^{-1} up to 2500 cycles. The cyclic voltammetry evaluation was performed between 0 and 1.2 V vs. RHE with sweep rate of 0.1 V/s in 1 M H_2SO_4 at room temperature. A carbon rod was used as the counter electrode and a radiometer® Hg/Hg_2SO_4 was used as the reference electrode. The printed electrodes were used as the working electrode in the electrochemical characterization and degradation studies. Argon purging was maintained during the measurements, with a constant flow of 0.2 mL/s. The experiments were carried out with an electrochemical workstation (Zahner® IM6e). The connection between the sample and the device was established with a 0.2 mm thick gold wire. Details of the calculations on electrochemical surface area (ECSA) and utilization (U) can be found in Section 3.2.

3. Results and Discussion

3.1. Electrode Morphology Revealed with HIM, SEM and TEM

In this section we compare the imaging results obtained with HIM, SEM and TEM techniques. Identical catalyst nanoparticles were used for the three types of microscopy. For HIM and SEM, 30 wt% of Nafion ionomer was included in the electrodes. The electrodes were imaged without any coating or pre-treatment. TEM was carried out on the pristine catalyst powder. The images and a summary of particle diameter distribution are presented in Figure 1.

Since TEM image contrast is formed by the electrons transmitted through the specimen, the atoms with higher atomic numbers appear in the images darker, because they scatter more electrons out of an imaging aperture. Therefore, platinum nanoparticles are seen as black dots and carbon supports are seen as gray grains in Figure 1A. Due to lack of ionomer, catalyst particles tend to agglomerate and stack on each other. The TEM pictures appear as 2-D images that reveal only a small part of the depth details.

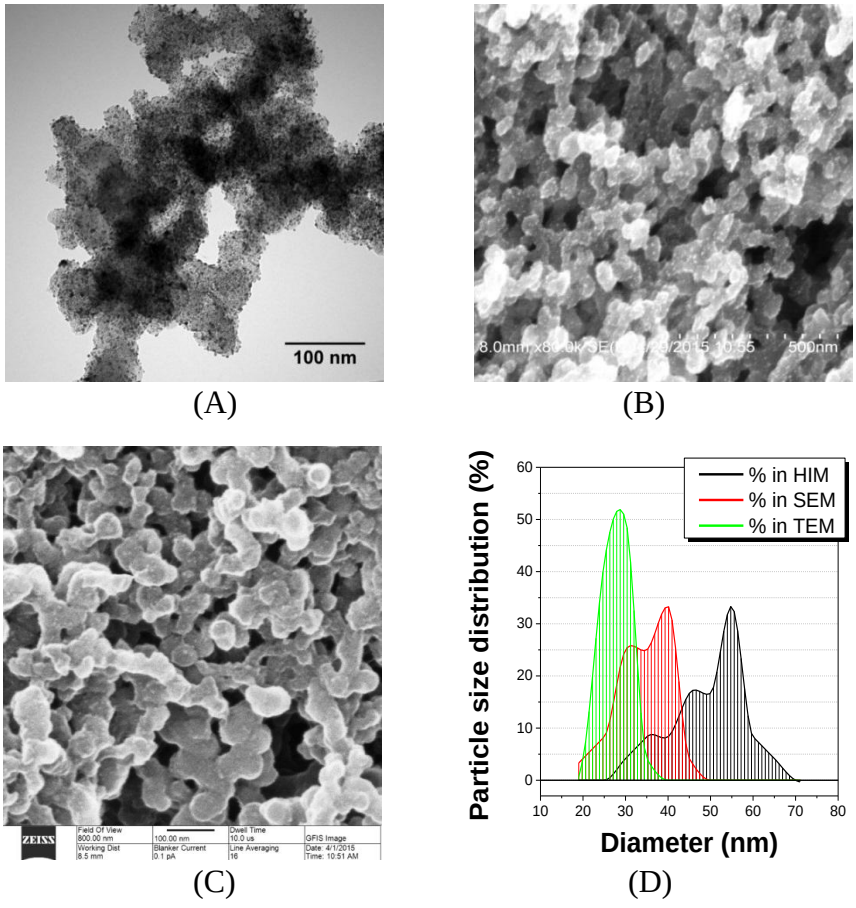

Figure 1. Electrode micrographs obtained with (A) TEM on the catalyst powder, (B) SEM on the electrode with 30% of ionomer and (C) high resolution HIM on the electrode with 30% of ionomer. The electrode with 30% of ionomer contains the same catalyst type as that used in TEM imaging. (D) Grain size distributions obtained from the TEM, SEM and HIM images.

SEM generates images by scanning the sample with a focused electron beam and detecting secondary electrons emitted by the sample atoms. Similar to TEM, atoms of high atomic numbers interact stronger with the electron beam, and as a result, generate more secondary electrons in contrast to the low-atomic number atoms. Therefore, platinum nanoparticles appear brighter than carbon support in SEM image (Figure 1B). The presented SEM picture also illustrates the image distortions specific to SEM, which manifest themselves as an elongation of the structural features in one of the in-plane directions. We have had persistent problems in obtaining undistorted images of our samples with SEM. Such type of distortions can be caused by many different reasons, such as mechanical drifts in the instrument. The distorsions could also result from movements of the sample features due to the local electrical charging, heating, accumulation of mechanical stress and radiation defects, or due to a combination of these factors during the exposure to the focused electron beam. In order to clarify this issue we have performed a range of SEM imaging trials on similarly mounted samples of high electrical conductivity. No distortions of this type were observed in these samples. Therefore, we exclude the mechanical drifts in our instrument as a cause for the observed distortions.

Figure 1C is a HIM image of the same sample that imaged in Figure 1B with SEM. It illustrates significant capability of HIM for revealing the authentic morphology of the electrode. First of all, we admit that the distortions specific to the SEM images are vanished. It demonstrates typical morphology of a standard electrode containing 30 wt% of Nafion ionomer and reveals Pt nanoparticles seen as bright dots. The density of Pt nano-particles found with HIM is substantially lower than that found with SEM. This difference can be explained by the fact that the most significant contribution to the image contrast in the case of HIM is given by the secondary electrons emmited essentially from the a few nanometers of the surface layer from the regions that are closer to the surface than in the case of SEM [26,27]. In other words, we attribute this discrepancy to the enhanced sensitivity of HIM to the surface layers and its relatively low sensitivity to buried features that are in our case Pt nanoparticles covered by Nafion layers and trapped in the pores of the high surface area carbon.

Figure 1D compares the results of the grain size analysis performed on sets of HIM, SEM and TEM images. The analysis of the HIM images resulted in a significantly larger average grain size (54 nm) and a much wider grain-size distribution than the analysis of the SEM images, which has given the averages size equal to about 37 nm. The smallest value of the average grain-size (of about 30 nm) was obtained from the analysis of TEM images. We recall that TEM was achieved on the pristine catalyst samples and the SEM and HIM images are from the samples impregnated with Nafion. Therefore, the difference in the grain size between the TEM and SEM/HIM images can be naturally attributed to the addition of the ionomer component. However, the SEM and HIM images were taken from the same samples and the difference in the average grain size corresponding to SEM and HIM is too large to be explained by experimental errors. We suggest that the above differences in the grain-size distribution are, to a large extent, related to morphology changes originated from radiation damage induced by the electron probe beam during our SEM imaging procedures. Radiation damage in polymers by electron beams and the role of this damage in generating image artefacts is well known and documented in literature (see for instance work [29] and references herein). The structural changes in polymers in this case can include bond-breaking, chain scission and cross-linking, volitile molecules generation, and as a result, mass loss and shrinking. As far as Nafion is concerned, there are only few publications on radiation damage of this material by electron beams. Shnaider [30] has found Nafion to be highly sensitive to the damage generated by an SEM

probe beam with an energy of 5 keV, which is the same as that used in our study. In particular, significant morphology changes have been observed in the Nafion samples dry-pressed at 140 ℃. These changes have been atributed to a combination of the electron beam induced atomic bond-breaking and a non-uniform microstructure of the Nafion samples. Similar structural non-uniformities and the related effects can occur in th Nafion-catalyst composite structures. Mass loss and phase separation have been found in studies of Nafion degradation under TEM imaging conditions [31].

To our knowledge, research of the radiation damage induced in Nafion by ion beams has until present been limited to ion implantation of heavy ions [32] and protons [33] into Nafion membranes. XPS analysis of the ion-implanted membranes revealed modifications of the surface molecular structure and an increase in the surface roughness. We found it to be very problematic to adapt these results to our observations, because the ion energy lost in nuclear collsions [26] is released entirely inside the Nafion membranes. On the contrary, due to very small thickness of Nafion layers in our structures, the dominant part of the He^+ ion energy dissipates inside the catalyst.

There is an additional fact that supports our expalnations: An extremely low probe-beam current (0.1 pA) has been used for imaging the electrode structures with HIM, and it was sufficient to achieve a very good signal-to-noise ratio. On the other hand, we have had to use the electron-beam probe currents of around 10 pA to generate SEM images of sufficient quality. Taking into account that, in our study, the landing energy (30 keV) of one He^+ ion is only 6 times higher than the landing energy (5 keV) of one electron, but the probe beam current is 100 higher in the case of HIM, we conclude that the energy density dissipated per one second in the electrode structure is substantially lower in the case of HIM.

Thus, we consider it to be most reasonable to conclude that HIM images reflect most accurately the actual surface morphology of the electrodes, and that the differences in the grain size distribution originate essentially from a lower level, and possibly, from a different character of the radiation damage caused by HIM imaging. Certainly, additional work is required to further clarify all the aspects of differences between the HIM and SEM results.

3.2. Electrochemistry

The electrochemical performance of the electrodes with different ionomer contents was evaluated in a three-electrode cell, and presented in Figure 2. The electrochemical surface area is calculated based on Coulombic charge transfer of monolayer atomic hydrogen adsorption, as shown in Eq. (1)

$$ECSA = \frac{Q}{[Pt] \times A \times C} \tag{1}$$

where, ECSA presents electrochemical surface area [$cm^2\ mg^{-1}$]; Q presents the charge for hydrogen desorption [mC]; [Pt] presents platinum loading, [$mg\ cm^{-2}$]; A presents geometric area [cm^2]; C presents the charge required to oxidize a monolayer of atomic hydrogen on Pt catalyst, C = 0.22 [$mC\ cm^{-2}$].

The utilization is calculated as the percentage of platinum surface area contributing in the electrochemical reaction in relation to its real geometric area according to Eq. (2)

$$U = \frac{ECSA \times \left(\frac{4}{3}\pi r^3 \rho\right)}{4\pi r^2} \times 100 = \frac{1}{3} \times ECSA \times r \times \rho \times 100 \quad (2)$$

where, U presents utilization [%]; r presents average radius of the platinum catalyst [m]; ρ presents density of platinum, 2.145 × 10^7 [g m^{-3}].

A series of typical cyclic voltammograms (CVs) based on 30 wt% Nafion ionomer is shown in Figure 2A; other CVs carry similar feature, but different degradation rate as summarized in Figure 2B. The electrochemical surface area was found to rise within the first 20 cycles and then gradually decrease until the end of the test at 2500 cycles. As we also observed in the earlier studies, the initial rising is due to a cleaning process and reorganization of the ionomer component; the declining is due to degradation of the platinum catalyst and collapse of the overall electrode structure [34,35,36].

Figure 2B summarizes the performance of the electrodes. An optimal composition was found to be of 30 wt% of ionomer, in terms of both maximum of the specific electrochemical surface area (or utilization) and durability (in terms of percentage of ECSA) after the 2500 cycles accelerated stress test. This superior electrode performance can be attributed to not only the high catalyst activation, but also to the efficient electrode structure that is further characterized in the following paragraphs.

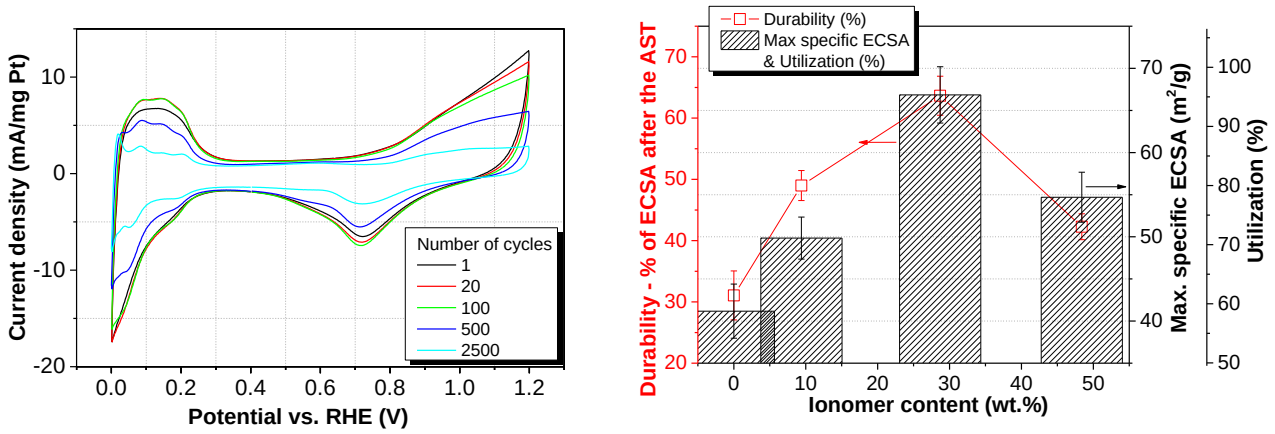

Figure 2. Electrochemical performance of the electrode in ex-situ test. (A) Typical cyclic voltammograms of the electrode containing 30 wt% Nafion after different cycles, and (B) is a summary of ECSA, utilization and durability in terms of percentage of the initial ECSA after the AST of the electrodes with different ionomer content.

3.3. Electrode Morphology at Nano-scale

As it was shown by the electrochemical measurements, the identical catalyst behaves significantly different in the electrodes of different ionomer content. The structure of these electrodes before and after AST was characterized in detail with the high resolution HIM.

Figures 3A–3D compare the pristine electrodes with ionomer content of 0, 10, 30 and 50 wt%. There are clear indications that with increasing ionomer content, a thin layer of ionomer film is formed on the catalyst particles surface and the film thickness increases. The appearance of the thin film is indicated by a blurring contour over the carbon particle edges. This observation is in a good

agreement with the results of our earlier adsorption studies, which revealed strong affinity between the ionomer and the catalyst particles [11,37]. Increased ionomer content occupies a larger volume of the free space in the catalyst structure; this results into a higher degree of isolation of the catalyst particles from each other and decrease in the pore volume from 27 to10% (see Figure 4).

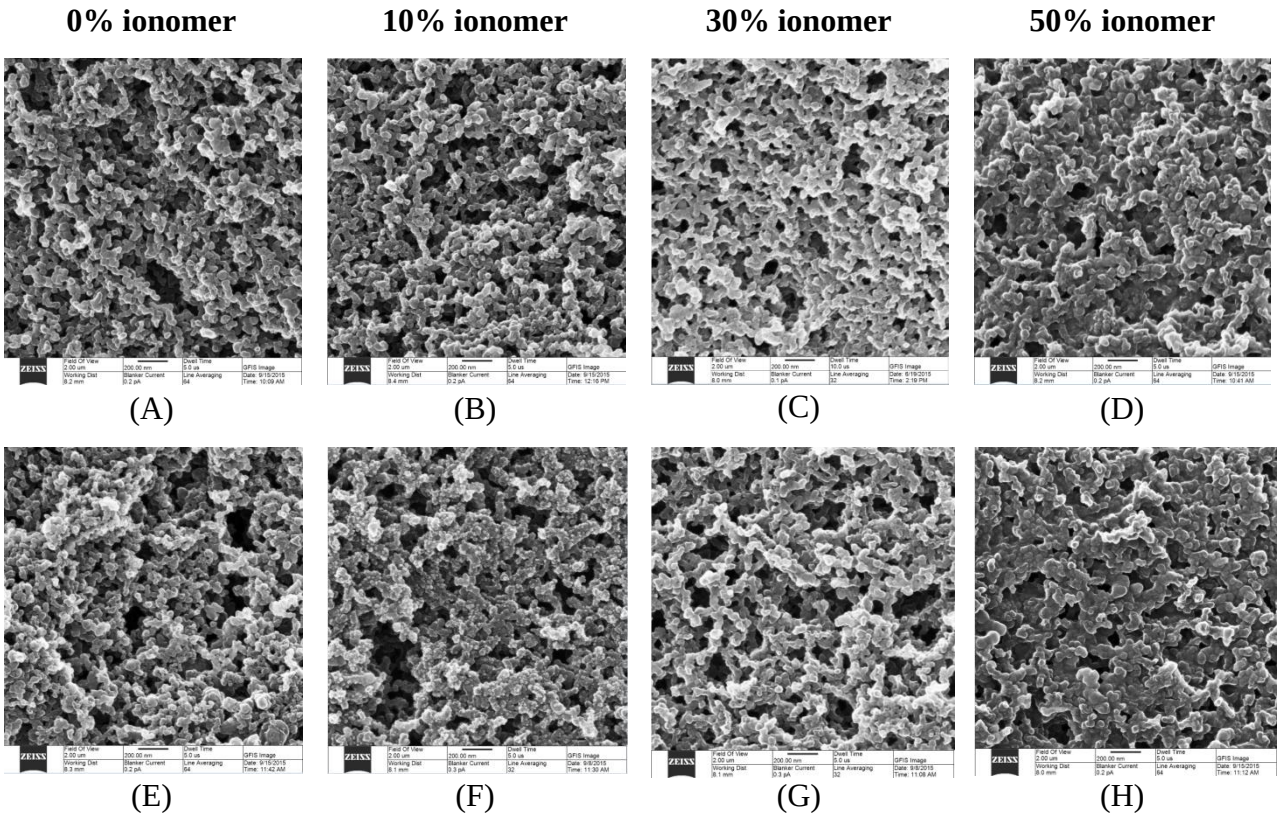

Figure 3. HIM images of the electrodes of different Nafion ionomer content. (A) to (D) are images before the AST and (E) to (H) are corresponding images after the AST.

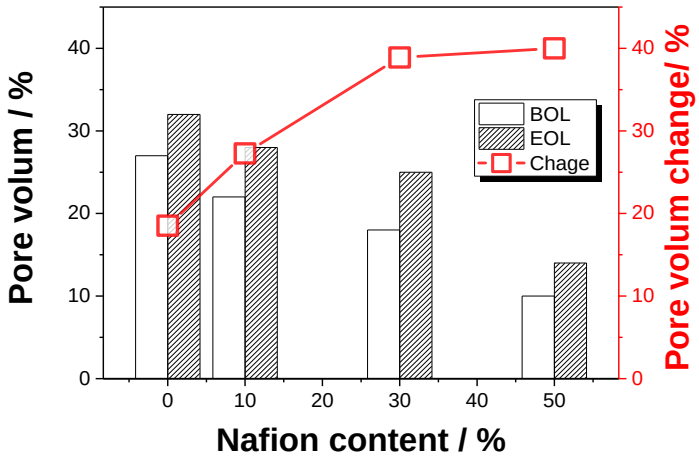

Figure 4. The electrode pore volume and change in this volume as functions of the Nafion content. The pore volume values are based on the analysis of HIM images.

Similar to the pristine electrodes, the accelerated stress tested electrodes with different ionomer content also carry distinctly different morphology (see Figures 3E to 3H). In general, the film structure reflects the ionomer content. Moreover, the AST electrodes carry 18 to 40% higher porosity than the corresponding pristine electrodes. The porosity change for the sample with 0% of ionomer content indicates carbon corrosion, which is a known degradation mechanism [38] in polymer fuel cells. For the ionomer-containing electrodes, degradation of the Nafion component in electrode structure can be a dominant degradation mechanism. Here, we should point out that the estimation of the electrode pore volume is based on the HIM images taken from the local microscopic regions. This estimate may be different from macroscopic estimates based on such techniques as permeation, gas adsorption (e.g., BET) or porosimetry [39].

Moreover, we should point out that our electrochemical AST was carried out at ambient pressure (plus ignorable hydrostatic pressure). This allows free morphology change of the electrode materials without any external mechanical stress. This leads to the consequence that once any electrode component (either carbon or proton conductor) is degraded, empty space appears as additional porosity. Therefore, after the accelerated stress test in this work, porosity of the electrodes generally increases.

This observation is not in conflict with earlier reported porosity decrease in fuel cell AST [40,41]. In most fuel cell configurations, to ensure stable contact, good sealing and high performance, single and stack cell inevitably use compressive or clamping pressure with spring load up to 70 bars [42,43] as well as pressurized gas supplies. The local pressure experienced at catalyst layer can be huge. Once the electrode component is degraded, instead of leaving empty space in the electrode, the electrode structure collapses and becomes more compact morphology; this leaves electrode apparent porosity decrease.

Figure 5 shows the samples of Figure 3 at a higher magnification to reveal fine details of the structure. In addition to the formation and growth of the Nafion film on the catalyst surface with increase in the ionomer content, we observe formation and growth of the membrane-like structures between the catalyst particles (see Figures 5A to 5D). In general, maximization of the contact area between the proton conductive polymer and the catalyst increases the triple-phase-boundary (TPB) and is a common strategy in PEMFC electrode design [44]. On the other hand, when an excess of the polymer is impregnated, such as in the case of 50% ionomer, a part of it is working as an electrical insulator and mass transport barrier. Therefore, the formation of the thick Nafion layers and the membrane structures is in a good agreement with the results of electrochemical measurements discussed in Section 3.2.

The images taken after the AST (Figures 5E to 5H) show additional small grains (8 to12 nm in diameter) formed in the electrodes containing 10 and 0 wt% of ionomer during the accelerated stress test. The grains are most likely platinum particles formed via Ostwald ripening. This phenomenon appears more pronounced in 10% electrodes than in 0% electrodes. This difference may be due to the differences in Pt migration and dissolution in the electrodes with and without ionomer, or by different degree of the carbon corrosion in these electrodes, or by a combination of these factors.

Formation of the additional grains was not observed in the electrodes of higher ionomer content (in samples with 30 and 50% of Nafion). This observation may be explained by the fact that the catalyst particles in these layers are covered by thicker polymer layers, and therefore, they can better tolerate the stress condition, that is consistent with the AST results presented in Section 3.2. The catalysts under the thick ionomer layer can be less degraded (as shown in Section 3.2) and the

dissolved Pt ions are prevented from re-deposition on the electrode surface due to lack of Pt nuclei or carbon support substrate.

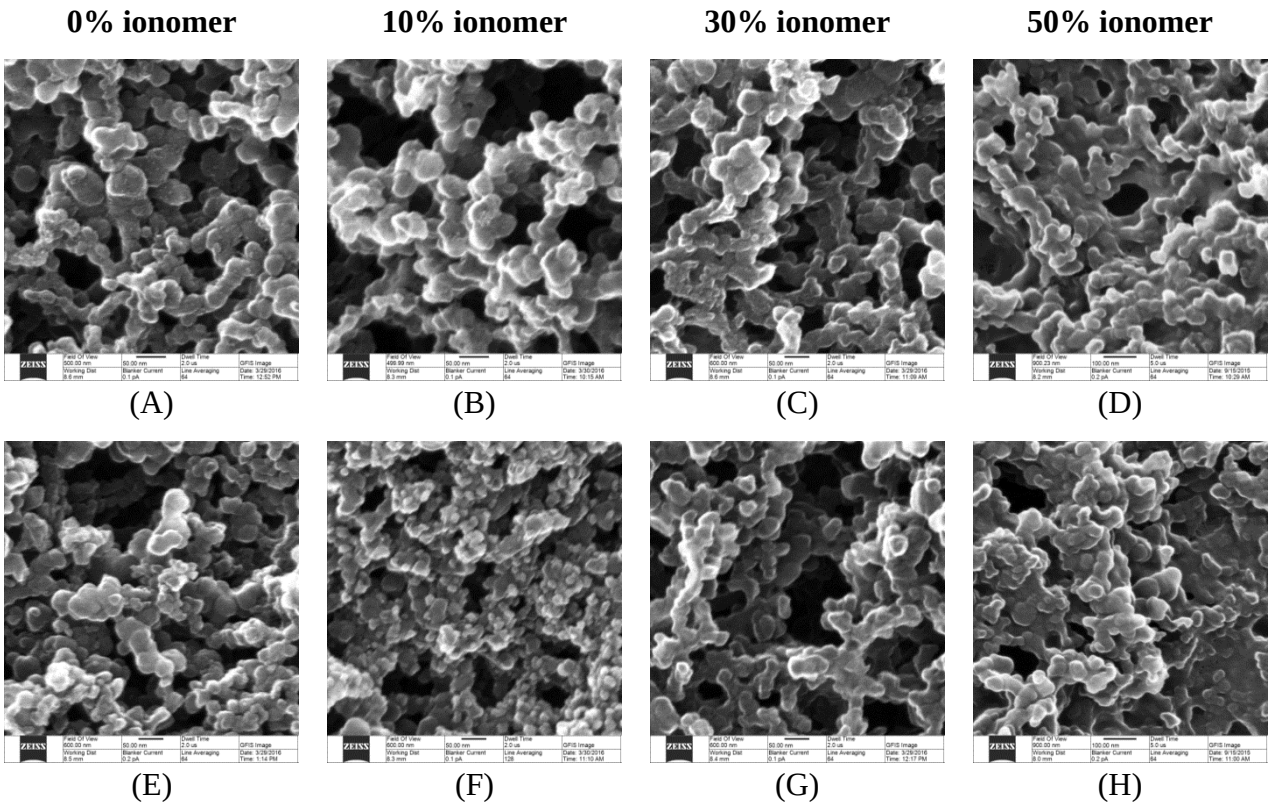

Figure 5. High magnification HIM images of electrodes of different Nafion ionomer content. (A) to (D) are images before the AST and (E) to (H) are corresponding images after the AST.

3.4. Electrode Morphology at Micro-scale

Due to the choice of solvent for the electrode ink and the processing procedure, cracks dividing the electrodes to patches were regularly observed in all the electrodes. The formation of the cracks is attributed to the tensile mechanical strain generated in the electrodes during the solvent evaporation process. Selecting a solvent with a lower boiling point and slowing down the drying procedure are reported to be effective strategies for manipulating the electrode surface macro-morphology [45]. The micrographs in previous Figure 3 were all taken from the inside regions of the patches. In the following low magnification images, the focus is placed at the crack regions. The results of preliminary examinations of the electrode surface are available in the supplementary material (see Figure S1).

Figures 5, 6A–6D illustrate crack regions of the pristine electrodes. The width of the cracks was found in a range of about 5 to 20 μm. Inside the cracks, very thin fibers with diameter in a range from about few tens to hundred nanometres were readily observed between the patch walls. The observed density of the fibers tends to increase with increasing the amount of the ionomer content in the electrodes. The fibers were not found in the electrodes without ionomer. This strongly suggests that the fiber structure is composed of Nafion polymer component originating from the ink ingredient.

The polymer fiber structures are most likely formed during the crack formation process. Though not intentionally designed, the polymer fibers strengthen the catalyst layer by connecting between the patch walls and reinforce the entire electrode structure. This is especially important for the mechanical stability of the electrode edges, as well as proton conduction and distribution. Figures 6E to 6H illustrate crack regions of the stressed electrodes. There is a significant reduction of the fiber density between the patch walls. This may be partially responsible for the reduction of the electrode performance after the electrochemical accelerated stress test.

Capturing quality images of the polymer fibers with SEM appeared to be a serious challenge, because during image acquisition, the electron irradiation destroys the fibers quickly and to a very large extent. Similar effects were observed during acquisition of the fiber images with HIM. The rates of the fiber destruction in the case of HIM however were significantly lower than in the case of SEM. This is one of the additional advantages of HIM in application to imaging of composite materials prone to radiation damage.

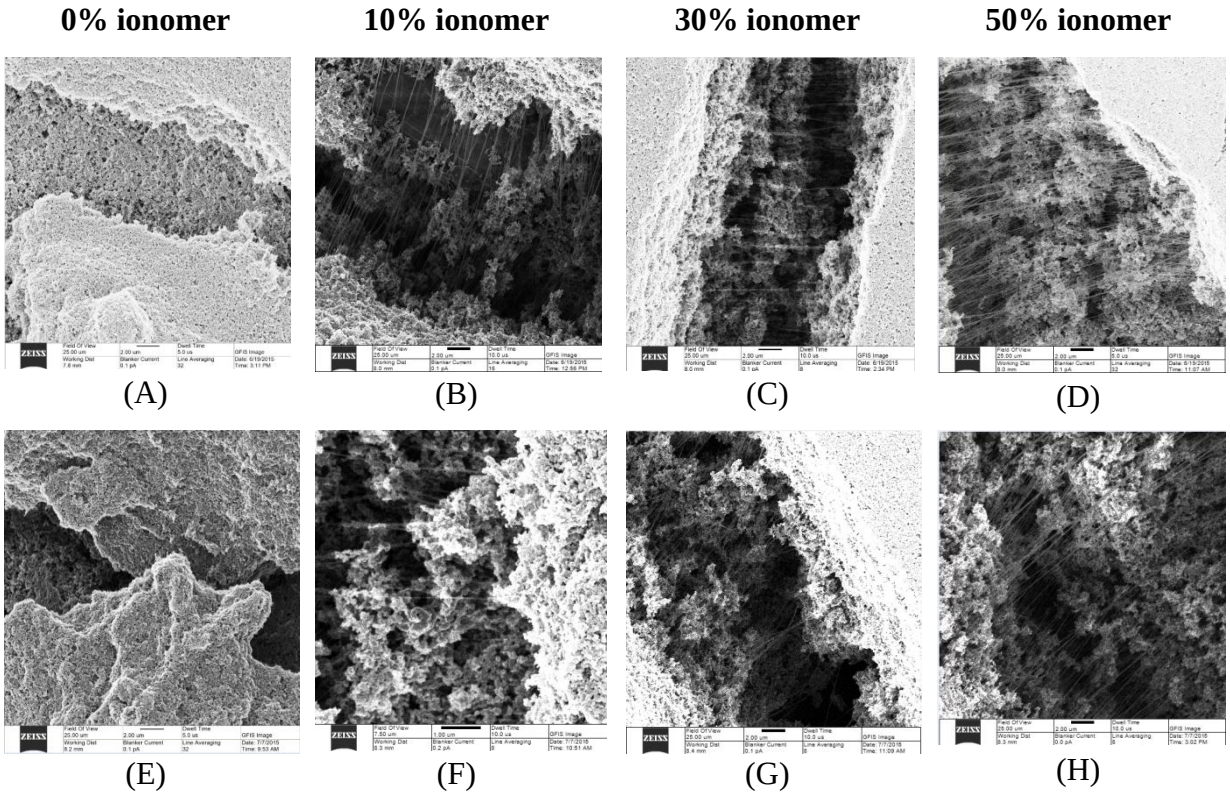

Figure 6. HIM images at low magnification of electrodes with different ionomer content. (A) to (D) are images before the AST and (E) to (H) are corresponding images after the AST.

3.5. Electrode Morphology due to Hot-pressing

As the only appropriate joining technology for PEMFCs, the hot-pressing (or lamination, welding) promotes coalescence of the bonding partners by applying pressure and heat to the interface. During lamination, the proton conductive membrane is sandwiched between two pieces of the electrodes to form a close contact. The conditions of the hot pressing, such as pressure, temperature

and duration play an important role in the electrode performance. Many groups have devoted their great efforts to understanding the key details of this process [46,47,48]. Our group has also carried out intensive studies of the lamination effects, with a focus on the catalyst performance [35]. However, any direct characterization of the hot-pressed electrodes with the microscopic techniques has so far not been reported in the literature.

The HIM images in Figure 7 show a sample of the electrode with 30 wt% Nafion ionomer before and after hot-pressing at 150 ℃, with a pressure of 7 bar and for 3 min. The laminated electrode in this images appears to be more compact compared to the pristine electrode, which can be naturally explained by a significant reduction in the electrode volume (by around 10% of the original thickness) [34] under the high temperature and high pressure lamination. This is also the major purpose of the lamination, to provide more intimate contact between the electrode components and electrode-electrolyte layers. Besides this, the average grain size in the hot-pressed sample is reduced, which is probably related to the polymer migration in the melted state and polymer dehydration. Further, in many areas the polymer component coalescences to reduce its surface area. Last but not least, the polymer component was found to form fiber-like structures with dimensions of a few nanometers and similar to those described in Section 3.4, but much thinner. These polymer fiber structures between the electrode grains can be interesting from the point of view of both the mechanical strength and proton conduction in the electrodes.

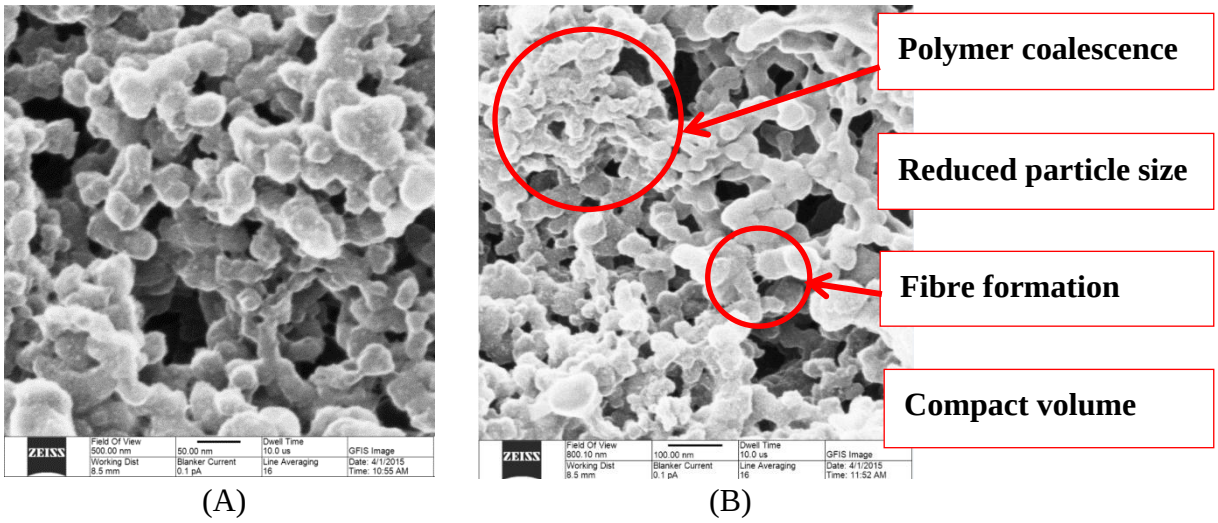

Figure 7. HIM images of the polymer fuel cell electrodes with 30 wt% of ionomer before (A) and after hot-pressing treatment (B).

4. Conclusion

Due to a range of advantages, in comparison to the other microscopy techniques, HIM appeared to be a very valuable tool for characterization of the morphology of PEMFC composite electrodes, including the surface and interface structures, porosity, and for post-mortem analysis of degradation mechanisms. The morphology of the pristine and electrochemically stressed electrodes containing the identical catalyst and different amounts of Nafion ionomer (0, 10, 30 and 50 wt%) was characterized at different length scales in a combination with the electrochemical measurements. The electrode morphology features revealed by HIM directly reflect changes in the polymer content,

consent the results of the electrochemical measurements and provide structure clarifications. The ionomer content was found to influence the morphology and the degree of degradation in the samples during the accelerated stress tests. The appearance of the additional small granular structure in the samples with zero and low ionomer content was observed and attributed to re-deposition of platinum particle controlled by Ostwald ripening. Lack of these structures in the samples with high polymer content is attributed to the formation of thick ionomer layers covering the catalyst particles. Fine polymer fiber structures were observed in both the electrode cracks and between the catalyst particles. These fibers can provide a better mechanical stability and a more efficient proton-conduction network in the electrodes.

Acknowledgements

Dr. Maryam Borghei is greatly appreciated for performing TEM. The authors appreciate the financial support from DuraPEM III (ForskEL J.No 2013-1-12064), UpCat (ForskEL J.No 2015-1-12315), and from the Danish Council for Strategic Research, Innovation Fond Denmark, through the 4M Centre (J.No 12-132710).

Conflict of Interest

The authors declare no conflict of interest.

References

1. Ren G, Ma G, Cong N (2015) Review of electrical energy storage system for vehicular applications. *Renew Sust Energ Rev* 41: 225–236.
2. Chang H, Wu H (2013) Graphene-based nanocomposites: preparation, functionalization, and energy and environmental applications. *Energ Environ Sci* 6: 3483–3507.
3. Guer TM (2013) Critical Review of Carbon Conversion in "Carbon Fuel Cells". *Chem Rev* 113: 6179–6206.
4. Chen Z, Higgins D, Yu A, et al. (2011) A review on non-precious metal electrocatalysts for PEM fuel cells. *Energ Environ Sci* 4: 3167–3192.
5. Gasteiger HA, Vielstich W, Yokokawa H (2009) *Handbook of Fuel Cells*, Chichester, England: John Wiley & Sons Ltd., 5–6.
6. Scofield ME, Liu H, Wong SS (2015) A concise guide to sustainable PEMFCs: recent advances in improving both oxygen reduction catalysts and proton exchange membranes. *Chem Soc Rev* 44: 5836–5860.
7. Suzuki T, Tsushim S, Hirai S (2011) Effects of Nafion® Ionomer and Carbon Particles on Structure Formation in a Proton-exchange Membrane Fuel Cell Catalyst Layer Fabricated by the Decal-transfer Method. *Int J Hydrogen Energ* 36: 12361–12369.
8. Kim KH, Lee KY, Kim HJ, et al. (2010) The effects of Nafion® Ionomer Content in PEMFC MEAs Prepared by a Catalyst-coated Membrane (CCM) Spraying Method. *Int J Hydrogen Energ* 35: 2119–2126.

9. Zhao X, Li W, Fu Y, et al. (2012) Influence of Ionomer Content on the Proton Conduction and Oxygen Transport in the Carbon-supported Catalyst Layers in DMFC. *Int J Hydrogen Energ* 37: 9845–9852.
10. Li W, Waje M, Chen Z, et al. (2010) Platinum Nanopaticles Supported on Stacked-cup Carbon Nanofibers as Electrocatalysts for Proton Exchange Membrane Fuel Cell. *Carbon* 48: 995–1003.
11. Ma S, Chen Q, Jøgensen FH, et al. (2007) ^{19}F NMR studies of Nafion^{TM} ionomer adsorption on PEMFC catalysts and supporting carbons. *Solid State Ionics* 178: 1568–1575.
12. Andersen SM, Borghei M, Dhiman R, et al. (2014) Interaction of multi-walled carbon nanotubes with perfluorinated sulfonic acid ionomers and surface treatment studies. *Carbon* 71: 218–228.
13. Andersen SM, Borghei M, Dhiman R, et al. (2014) Adsorption behavior of perfluorinated sulfonic acid ionomer on highly graphitized carbon nanofibers and their thermal stabilities. *J Phys Chem C* 118: 10814–10823.
14. Paul D, Fraser A, Pearce J, et al. (2011) Understanding the Ionomer Structure and the Proton Conduction Mechanism in PEFC Catalyst Layer: Adsorbed Nafion on Model Substrate. *ECS Trans* 41: 1393–1406.
15. Kongkanand A (2011) Interfacial Water Transport Measurements in Nafion Thin Films Using a Quartz-Crystal Microbalance. *J Phys Chem C* 115: 11318–11325.
16. Yu J, Jiang Z, Hou M, et al. (2014) Analysis of the Behavior and Degradation in Proton Exchange Membrane Fuel Cells with a Dead-ended Anode. *J Power Sources* 246: 90–94.
17. Ma S, Solterbeck CH, Odgaard M, et al. (2009) Microscopy Studies on Pronton Exchange Membrane Fuel Cell Electrodes with Different Ionomer Contents. *Appl Phys A-Mater* 96: 581–589.
18. Yakovlev S, Balsara NP, Downing KH (2013) Insights on the Study of Nafion Nanoscale Morphology byTransmission Electron Microscopy. *Membranes* 3: 424–439.
19. Scheiba F, Benker N, Kunz U, et al. (2008) Electron Microscopy Techniques for the Analysis of the Polymer Electrolyte Distribution in Proton Exchange Membrane Fuel Cells. *J Power Sources* 177: 273–280.
20. Radicea S, Oldani C, Merlo L, et al. (2013) Aquivion PerfluoroSulfonic Acid Ionomer Membranes: A Micro-Raman Spectroscopic Study of Ageing. *Polym Degrad Stabil* 98: 1138–1143.
21. Eastcott JI, Easton EB (2014) Sulfonated Silica-based Fuel Cell Electrode Structures for Low Humidity Applications. *J Power Sources* 245: 487–494.
22. Bautista-Rodríguez CM, Rosas-Paleta A, Rivera-Márquez JA, et al. (2009) Study of Electrical Resistance on the Surface of Nafion 115® Membrane Used as Electrolyte in PEMFC Technology Part I: Statistical Inference. *Int J Electrochem Sci* 4: 43–59.
23. Butler JH, Joy DC, Bradley G, et al. (1995) Low-voltage scanning electron microscopy of polymers. *Polymer* 36: 1781–1790.
24. Rodenburg C, Viswanathan P, Jepson MAE, et al. (2014) Helium ion microscopy based wall thickness and surface roughness analysis of polymer foams obtained from high internal phase emulsion. *Ultramicroscopy* 139: 13–19.
25. Notte J, Huang J (2016) The Helium Ion Microscope, In: Hlawacek G, Gölzhäuser A, *Helium Ion Microscopy*, Springer, 3–30.
26. Boden SA (2016) Introduction to Imaging Techniques in the HIM, In: Hlawacek G, Gölzhäuser A, *Helium Ion Microscopy*, Springer, 149–172.

27. Hlawacek G, Veligura V, Gastel R, et al. (2014) Helium Ion Microscopy. *J Vac Sci Technol B* 32: 020801.
28. Tintula KK, Jalajakshi A, Sahu AK, et al. (2012) Durability of Pt/C and Pt/MC-PEDOT Catalysts under Simulated Start-Stop Cycles in Polymer Electrolyte Fuel Cells. *Fuel Cells* 13: 158–166.
29. Egerton RF, Li P, Malac M (2004) Radiation damage in the TEM and SEM. *Micron* 35: 399–409.
30. Schneider R (2008) Scanning Electron Microscopy Studies of Nafion Deformation into Silicon Micro-Trenches for Fuel Cell Applications [PhD Thesis]. Princeton University, New Jersey.
31. Yakovlev S, Balsara NP, Downing KH (2013) Insights on the Study of Nafion Nanoscale Morphology by Transmission Electron Microscopy. *Membranes* 3: 424–439.
32. Hoffman EA, Fekete ZA, Korugic-Karasz LS, et al. (2004) Theoretical and experimental X-ray photoelectron spectroscopy investigation of ion-implanted nafion. *J Polym Sci Pol Chem* 42: 551–556.
33. Lee J, Hwang I, Jung C, et al. (2016) Surface modification of Nafion membranes by ion implantation to reduce methanol crossover in direct methanol fuel cells. *RSC Adv* 6: 62467–62470.
34. Andersen SM, Skou E (2014) Electrochemical Performance and Durability of Carbon Supported Pt Catalyst in Contact with Aqueous and Polymeric Proton Conductors. *ACS Appl Mater Interfaces* 19: 16565–16576.
35. Andersen SM, Dhiman R, Larsen MJ, et al. (2015) Importance of Electrode Hot-Pressing Conditions for the Catalyst Performance of Proton Exchange Membrane Fuel Cells. *Appl Catal B-Environ* 172: 82–90.
36. Andersen SM, Grahl-Madsen L (2014) Understanding on Interface Contribution to the Electrode Performance of Proton Exchange Membrane Fuel Cells—Impact of the Ionomer Content. *Int J Hydrogen Energ* 41: 1892–1901.
37. Andersen SM (2016) Nano carbon supported platinum catalyst interaction behavior with perfluorosulfonic acid ionomer and their interface structures. *Appl Catal B-Environ* 181: 146–155.
38. Zhang S, Yuan XZ, Hin JNC, et al. (2009) A review of platinum-based catalyst layer degradation in proton exchange membrane fuel cells. *J Power Sources* 194: 588–600.
39. Yu H, Roller JM, Mustain WE, et al. (2015) Influence of the ionomer/carbon ratio for low-Pt loading catalyst layer prepared by reactive spray deposition technology. *J Power Sources* 183: 84–94.
40. Reiser CA, Bregoli L, Patterson TW, et al. (2005) A reverse-current decay mechanism for fuel cells. *Electrochem Solid-State Lett* 8: A273–A276.
41. Vielstich W, Gasteiger HA, Yokokawa H (2009) *Handbook of Fuel Cells: Advances in Electrocatalysis, Materials, Diagnostics and Durability: Part 2*, Wiley-Blackwell.
42. Li G, Tan J, Gong J (2014) Effect of Compressive Pressure on the Contact Behavior Between Bipolar Plate and Gas Diffusion Layer in a Proton Exchange Membrane Fuel Cell. *J Fuel Cell Sci Tech* 11: 041009.
43. Diedrichs A, Rastedt M, Pinar FJ, et al. (2013) Effect of compression on the performance of a HT-PEM fuel cell. *J Appl Electrochem* 43: 1079–1099.
44. Jeong B, Ocon JD, Lee J (2016) Electrode Architecture in Galvanic and Electrolytic Energy Cells. *Angew Chem Int Ed* 55: 4870–4880.

45. Kim YS, Welch CF, Mack NH, et al. (2014) Highly durable fuel cell electrodes based on ionomers dispersed in glycerol. *Phys Chem Chem Phys* 16: 5927–5932.
46. Fultz DW, Chuang PYA (2011) The Property and Performance Differences Between Catalyst, Coated Membrane and Catalyst Coated Diffusion Media. *J Fuel Cell Sci Tech* 8: 041010.
47. Okur O, Karadag CL, San FJB, et al. (2013) Optimization of Parameters for Hot-Pressing Manufacture of Membrane Electrode Assembly for PEM (Polymer Electrolyte Membrane Fuel Cells) Fuel Cell. *Energy* 57: 574–580.
48. Jia S, Liu H (2012) Cold Pre-Compression of Membrane Electrode Assembly for PEM Fuel Cells. *Int J Hydrogen Energ* 37: 1367–13680.

AIMS Press